# M3BA: A Mobile, Modular, Multimodal Biosignal Acquisition Architecture for Miniaturized EEG-NIRS-Based Hybrid BCI and Monitoring

Alexander von Lühmann*, Heidrun Wabnitz, Tilmann Sander, and Klaus-Robert Müller*, *Member, IEEE*

***Abstract*—*Objective:* For the further development of the fields of telemedicine, neurotechnology, and brain–computer interfaces, advances in hybrid multimodal signal acquisition and processing technology are invaluable. Currently, there are no commonly available hybrid devices combining bioelectrical and biooptical neurophysiological measurements [here electroencephalography (EEG) and functional near-infrared spectroscopy (NIRS)]. Our objective was to design such an instrument in a miniaturized, customizable, and wireless form. *Methods:* We present here the design and evaluation of a mobile, modular, multimodal biosignal acquisition architecture (M3BA) based on a high-performance analog front-end optimized for biopotential acquisition, a microcontroller, and our open-NIRS technology. *Results:* The designed M3BA modules are very small configurable high-precision and low-noise modules (EEG input referred noise @ $500$ SPS 1.39 $\mu V_{pp}$, NIRS noise equivalent power $NEP_{750\,nm} = 5.92\,pW_{pp}$, and $NEP_{850\,nm} = 4.77\,pW_{pp}$) with full input linearity, Bluetooth, 3-D accelerometer, and low power consumption. They support flexible user-specified biopotential reference setups and wireless body area/sensor network scenarios. *Conclusion:* Performance characterization and *in-vivo* experiments confirmed functionality and quality of the designed architecture. *Significance:* Telemedicine and assistive neurotechnology scenarios will increasingly include wearable multimodal sensors in the future. The M3BA architecture can significantly facilitate future designs for research in these and other fields that rely on customized mobile hybrid biosignal acquisition hardware.**

***Index Terms*—Electroencephalography (EEG), hybrid brain–computer interface (BCI), mobile, modular, multimodal biosignal acquisition architecture (M3BA), multimodal, near-infrared spectroscopy (NIRS), wireless body area network (WBAN), wireless body sensor network (WBSN).**

Manuscript received April 1, 2016; revised May 17, 2016 and July 19, 2016; accepted July 19, 2016. Date of publication September 9, 2016; date of current version May 15, 2017. The work of A. von Lühmann was supported by the BIMoS Graduate School, Technical University of Berlin. The work of K.-R. Müller was partially supported by the National Research Foundation of Korea funded by the Ministry of Education, Science, and Technology in the BK21 program and by the German Research Foundation under Grant DFG MU 987/6-1, Grant SPP 1527, and Grant MU 987/14-1. *Asterisk indicates corresponding authors.*

*A. von Lühmann is with the Machine Learning Department, Technical University of Berlin, Berlin 10623, Germany (e-mail: a.vonluehmann@campus.tu-berlin.de).

H. Wabnitz and T. Sander are with Physikalisch-Technische Bundesanstalt.

*K.-R. Müller is with the Machine Learning Department, Technical University of Berlin, and also with the Department of Brain and Cognitive Engineering, Korea University (e-mail: klaus-robert.mueller@tu-berlin.de).

This paper has supplementary downloadable material available at http://ieeexplore.ieee.org.

Digital Object Identifier 10.1109/TBME.2016.2594127

## I. Introduction

INITIATED by wearable computers and smartphones with increasing computational capacity, there is an ongoing growing trend toward wearable body sensors, telemedicine, and pervasive healthcare [1], [2]. Acquisition hardware and sensors become increasingly miniaturized. Communication technology rapidly develops toward extremely low latencies in conjunction with high availability, reliability, and security (tactile internet). As a result, wireless body sensor networks (WBSNs) can incorporate an increasing number of biosignal modalities and integrate contextual environmental information.

In another domain, brain–computer interfaces (BCI), the range of—mainly static—applications has been extended substantially by combining BCI with various physiological and technical signals [3]. Also, functional near-infrared spectroscopy (fNIRS) joined the modality set used for multimodal BCI or enhancement of electroencephalogram (EEG)-based BCI [4], [5]. fNIRS is a noninvasive optical technology that makes use of at least two wavelengths in the near-infrared (NIR) spectrum of light for the local measurement of oxy- ($O_2Hb$) and deoxy- (HHb) hemoglobin concentration changes in cortical brain areas. Such multimodal so-called hybrid BCIs [6], [7] illustrate the potential to significantly increase the amount of exploitable information by assessing both shared and complementary information in the signals measured. Furthermore, this potentially enables more robust approaches toward operation under real-life conditions.

These advancements in wearable devices and BCI also influence new research areas linked to either domain: Neuroergonomics [8], [9] and adaptive neurotechnology research [10]–[12] focus on the use of both brain and body biosignals in the design of more comprehensive human–machine interfaces. Those interfaces have the potential to improve work environments, efficiency, and security and advance the understanding of brain function in real-world scenarios.

Our work contributes to the endeavor of advancing BCI technology further beyond traditional applications: toward out of the lab use and into a broader context of wearable sensor applications, using hybridization and contextualization. While today

0018-9294 © 2016 IEEE. Translations and content mining are permitted for academic research only. Personal use is also permitted, but republication/redistribution requires IEEE permission. See http://www.ieee.org/publications_standards/publications/rights/index.html for more information.

miniaturized mobile EEG devices are commercially available and have successfully been used in mobile BCI applications [13], only few mobile fNIRS devices exist on the market and in research (e.g., [14], [15]). The majority of these are portable, but require a backpack. We previously developed a state-of-the-art (for a review see [16]) highly miniaturized wireless open-source fNIRS device, i.e., the openNIRS [17], for integration into various mobile hardware applications. Regarding hybrid neurotechnology for the joint acquisition of fNIRS and electrophysiological signals such as EEG, electrocardiogram (ECG), or electromyogram (EMG), there are currently no instruments on the market and only very few in research. While separate EEG and fNIRS tabletop systems are commonly combined in stationary experiments (e.g., [5], [18]), mobile scenarios require researchers to develop their own hybrid devices. Due to the necessity of interdisciplinary expertise in the hardware design and potentially high costs and development time, very few custom instruments have been published so far: One of the first mobile EEG-fNIRS hybrids was presented by Lareau *et al.* in 2011 [19] and its next generation by Sawan *et al.* in 2013 [20]. Both provide high channel count and performance, but their size requires the use of a backpack ($14 \times 14 \times 5\,\text{cm}^3$). In 2014, Zhang *et al.* [21] published a wearable hybrid with fNIRS, single-channel ECG, and accelerometer (ACCEL) for ambulatory long-term hemodynamic and systemic monitoring, but no EEG. In 2013, Safaie *et al.* presented a sophisticated multichannel device for investigation of interactions between neuronal electrical and regional microcirculation activity [22]. It features high-performance fNIRS, EEG, and ACCEL in a tiny volume ($3.5 \times 8 \times 1\,\text{cm}^3$). Aiming to enable wide-range out-of-lab use of the existing technology, it would furthermore be desirable to integrate the following features into one hybrid device:

1) phase-sensitive (lock-in) detection (PSD) of optical signals, which increases robustness against changing ambient light in mobile applications;
2) simultaneous acquisition of different bioelectrical signals with distinct references, e.g., ECG or EMG together with EEG;
3) optimization/evaluation of fNIRS switching crosstalk into the bioelectrical input channels (increasingly important with higher miniaturization);
4) simultaneous sampling of both bioelectrical and biooptical signals by a shared detector branch to decrease jitter between modality samples;
5) a flexible, easy to program, powerful onboard controller for software customization in stand-alone scenarios.

We present here our novel architecture for a new generation of highly customizable mobile, hybrid biooptical/bioelectrical designs that are compatible with WBSN scenarios. Using a shared analog front-end (AFE) and a powerful microcontroller, we integrate the above features, improve resolution (24 versus 16 bit in above devices), decrease costs, and, at the same time, further miniaturize beyond previous approaches ($4.2 \times 4.2 \times 0.6\,\text{cm}^3$). While the architecture works for a variety of signals and applications, we dedicate our instrument to the use in hybrid neurotechnology solutions, in particular BCI and neuroergonomics. We focus on fNIRS and EEG signals and support within the same device ACCEL, ECG, and EMG as additional modalities, with a separate reference for the latter. In the presented architecture, we also show how to use functional units from our openNIRS design to effectively create hybrid technology for acquisition of both electrical and optical biosignals. The present work does not deal with multimodal signal processing for parameter extraction or artifact suppression, this is left for future work. By sharing the architecture and corresponding characteristics in this paper, we hope to facilitate future designs by researchers in related fields.

In Section II, we illustrate the instrumentation concept and hardware architecture (see Section II-A), elaborate on the methods and phantoms used for the hardware performance characterization (see Section II-B), and describe the methods applied to acquire physiological data in *in-vivo* studies (see Section II-C). Section III covers the respective results: The instrument (see Section III-A), its optical and electrical characteristics (see Section III-B), and physiological validation (see Section III-C). In Sections IV and V, we discuss the results and conclude with an outlook on future work.

## II. Methodology

### A. Instrumentation

***1) Concept:*** To illustrate the system concept and scope of applications for the mobile, modular, multimodal biosignal acquisition (M3BA = "MEBA") device, Fig. 1 shows an exemplary hybrid WBSN BCI scenario.

While the detailed scenario and corresponding BCI studies are not in the scope of this paper, the setup exemplifies a typical use case, for which the modules were designed. Necessary for that are, among others, modularity, mobility, miniaturization and multimodality, scalability, and reconfigurable references. Also, the scenario implies the resulting potential for multimodal signal analysis approaches.

A single M3BA module provides $4 + 2$ channels for bioelectrical signal acquisition, which are designed for high-precision acquisition of EEG signals and can also be used for ECG, EMG, and EOG recordings. Four channels derive signals against a fixed common reference. The additional two channels can be used for derivation against the same common electrode or (via microswitch) against another independent reference. Each module also has two optical detectors and emitters and thus provides $4 + 2$ fNIRS channels, where the $+2$ channels are available when neighboring M3BA modules share emitter–detector pairs in a time-division multiple-access (TDMA) manner. Additionally, each module incorporates a 3-D accelerometer for acquisition of acceleration data. Electrodes and optodes can but do not have to be fixed to the module. Thus, the module can but does not have to be worn "on site"; depending on the application, headgear or caps could be used.

In the example scenario in Fig. 1, three modules M1–M3 are combined for simultaneous measurement of EEG, fNIRS, EMG, and ECG: M1 and M2 and one (detached) optode pair of M3 measure eight EEG and 13 fNIRS channels over the left somatosensory cortex, while M3 measures two EMG channels at the neck and two ECG channels on the chest. M1 and M2

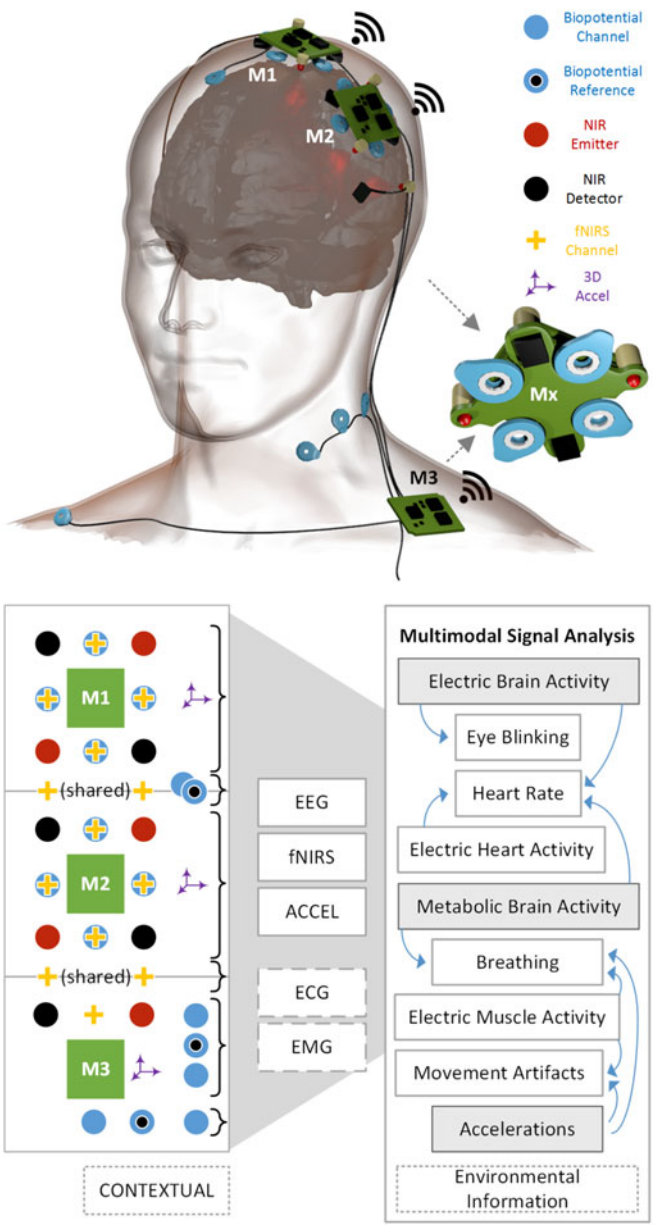


Fig. 1. Multimodal modular concept and example scenario: Modules ($M_{x=1\ldots3}$) can be combined to increase fNIRS channel count and number of modalities acquired synchronously. Each module provides 4+2 bioelectrical and 4+2 biooptical signal acquisition channels and one 3-D accelerometer. Multimodal signal analysis allows extraction of shared and complementary information in the set.

share a reference and ground electrode and make no use of the four bioelectrical channels that are additionally available. M3 uses the available reference split for the independent acquisition of EMG and ECG. M1, M2, and M3 share emitter/detector resources and thus create four shared fNIRS channels. Optionally, the modules can share a physical (nonwireless) interface for common time-critical signals such as a shared sampling clock and fNIRS channel control signals and—as in the case of M1 and M2—a common reference. In the standard case, this is established by flat ribbon wires with microcable-to-pcb connectors. All modules acquire movements (speed changes) via their 3-D accelerometer.

The resulting set of synchronously acquired (bio)signals enables a variety of new approaches for multimodal signal analysis and robustifying against (movement) artifacts. There has been an increasing number of novel methods that try to relate and optimize the amount of extracted information from the set that is shared or complementary in the single modalities (such as group independent component analysis methods [23], kernel cross correlation analysis [24], and multimodal source power correlation [25], [26]). The usage and exploration thereof exceed the scope of this hardware-oriented paper and will be subject of future work. However, since the idea of multimodality is inherent to the system concept, we briefly point out some potential benefits in a nonconservative BCI perspective (using the brain signals as one but not the only input): In single modality analysis (physiological or environmental), artifacts are usually to be suppressed maximally. However, when several modalities are combined in the analysis procedure, physiological and movement induced artifacts can be identified, suppressed, or extracted more easily. When extracted, they can also be used as additional parameters (such as heart rate, eye blinking frequency, etc.) for user state estimation in neuroergonomics or passive BCI scenarios. Typical examples for this are 1) the time-locked artifacts from heart activity as ECG in the EEG and pulse waves in fNIRS recordings and 2) respiratory or movement-related artifacts in EEG (EMG interference or electrode shifts) and fNIRS (modulation of oxy/deoxyhemoglobin signals and optode shifts) that are locked to synchronously acquired accelerometer data. See Section III-C2 for qualitative data that illustrate this.

***2) System Hardware Architecture:*** The hardware architecture (see Fig. 2) was designed to concord with the system concept and to provide high system performance, precision, and user safety.

When designing a new generation miniaturized hybrid instrument for bioelectrical and biooptical measurements, attention has to be paid on how to implement these hybrids such that high precision can be achieved and crosstalk between the signals and crosstalk from digital components in the mixed-circuit design is minimized. Here, essential advantages of unified hybrid approaches opposed to the combination of two separate instruments are both the synchronicity of the acquisition and a common ground that allows more sophisticated consideration of current paths and fields to minimize noise and electrical crosstalk. Especially considering miniaturization and precision aspects in a mixed-circuit design, we solved this by using a common AFE integrated circuit for both signal types.

The M3BA hardware architecture is based on the high-precision circuit ADS1299 [27] from Texas Instrument, which is a very low-noise ($1\ \mu\mathrm{V}_{\mathrm{pp}}$(70-Hz BW)) 24-bit Delta-Sigma AFE with eight differential inputs optimized for EEG biopotential measurements. It provides many peripheral features such as programmable gain amplifiers (PGAs, $G = 1 - 24$), configurable sample rate (250 SPS $-$ 16 kSPS), a built in bias-drive amplifier, and a multifunctional input multiplexer (MUX). Furthermore, an extensive documentation of electrical and performance characteristics for biopotential measurements is provided by the manufacturer. We embedded the AFE in a framework made up of a powerful 32-bit ARM Cortex M4 microcontroller,

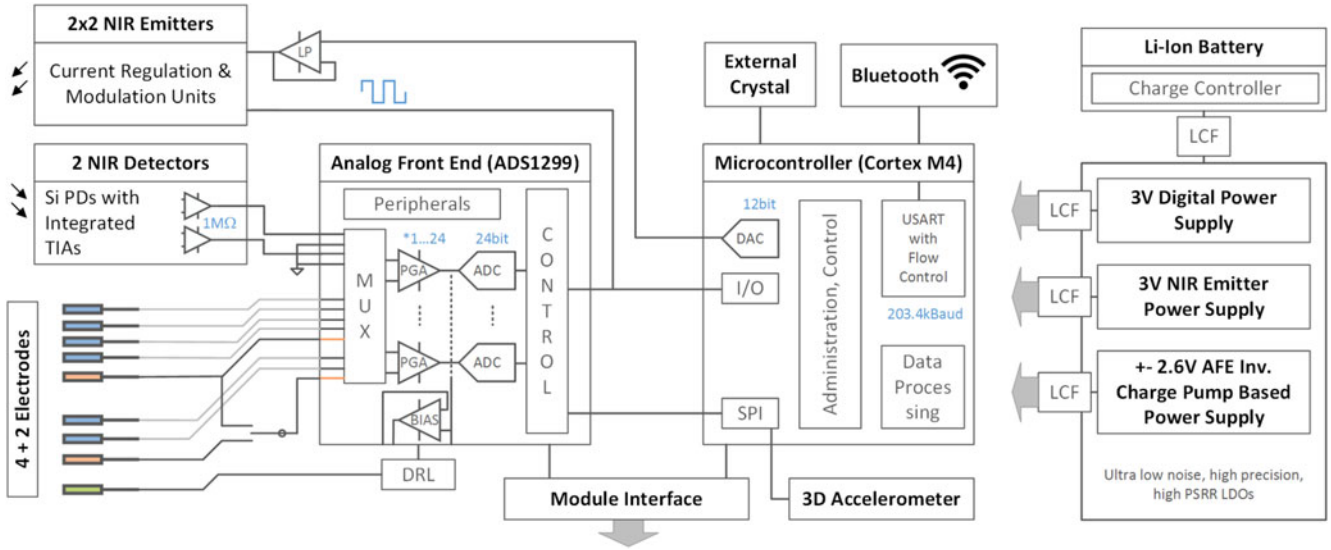


Fig. 2. System hardware architecture: Stand-alone high-precision hybrid biosignal acquisition by utilizing an ultralow noise biosignal AFE and a powerful Cortex M4 microcontroller together with improved NIR emitter and detector units from the openNIRS design [17]. 4+2 differential biopotential inputs [blue: meas., orange: switchable reference, green: ground (configurable driven right leg)]. All critical components are buffered and supplied individually by ultralow noise, high power supply rejection ratio (PSSR) low-dropout regulators (LDO) from a charge-controlled Li-ion battery. Communication and data transfer via integrated BTM.

an ADXL343 accelerometer, and enhanced functional units for NIR light emission and detection, which are inspired by our previously published modular openNIRS technology (refer to [17] for more details).

1) The configurable NIR light emitter units use dual-wavelength light-emitting diodes (LEDs) with 750 and 850 nm (Epitex L750/850-04A) that are stabilized and modulated by custom high-precision OpAmp and FET-based circuits for current regulation and modulation. This increases accuracy and robustness against radiation intensity fluctuations due to voltage variations or temperature changes and enables square-wave modulation for phase-sensitive (lock-in) detection.
2) The NIR light detector units are based on Si-photodiodes (Burr-Brown OPT101) with integrated transimpedance amplifiers. The selection is a tradeoff between safety and minimization aspects (lower supply voltages and smaller size), responsivity (0.45 A/W @650 nm), noise minimization and bandwidth (14 kHz) for phase-sensitive detection. In the openNIRS design, the analog detection was based on an analog lock-in detection circuit. Here, we minimized attenuation by phase shifts, size, cost, and number of components by performing phase-sensitive demodulation on the microcontroller in the digital domain.

The eight differential AFE signal inputs are split into two channels that measure the single-ended optical time-division multiplexed NIRS signal against analog system GND and $4+2$ differential biopotential channels that are measured against a split or common reference (selectable via microswitch). In this way, the AFE fuses the high-precision measurements of both analog signal types. Configuration, control, processing, and communication tasks are performed by the Cortex M4 microcontroller running at 120 MHz with an external crystal for jitter minimization. In particular, it performs

1) data processing and retrieval from AFE and Accelerometer (via serial peripheral interface);
2) configuration of AFE (PGA, MUX, sample rate, etc.);
3) adjustment, regulation, and modulation of NIR LED currents. For adjustment, a filtered internal 12-bit digital-to-analog converter signal is used as regulator command variable;
4) NIRS channel control and timing, digital lock-in demodulation of optical signals;
5) communication with a host (e.g., notebook) [via flow-controlled ring-buffered USART Bluetooth module (BTM)] and other modules (physical interface for timing and control);
6) power management and supply control.

For minimization of noise and electrical crosstalk between analog signals but also between the analog and digital circuits, the architecture was carefully designed considering the best practice for mixed-signal, multilayer, and multipower supply designs. To maximally decouple the functional analog and digital units in the instrument, the LED emitter units, the bipolar analog detector, and AFE circuits and the digital components (microcontroller, accelerometer, digital AFE side, etc.) are supplied separately by ultralow noise, high precision, and high Power Supply Rejection Ratio (PSRR) low-dropout regulator-based power supplies and are additionally buffered with *LC*- and ferrite low-pass filters. The six-layer printed circuit board (PCB) was layouted with split analog, digital, and supply planes in a star ground (GND) manner, shielding, via stitching and return current optimization techniques, among others. The instrument is supplied by a single Li-ion battery with integrated protection circuit module and provides a charge controller for fast recharging via USB. As M3BA is completely wireless and running on voltages $<3.7$ V, user safety and power consumption issues are dramatically decreased: For fault conditions, current-limiting

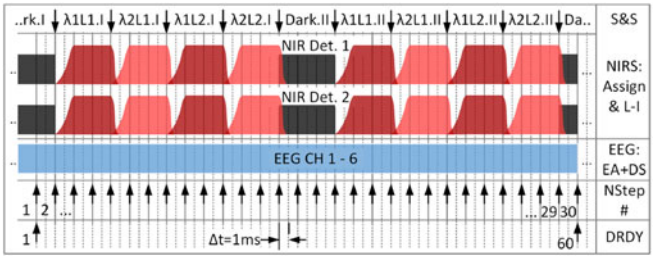


Fig. 3. Hybrid NIRS & EEG acquisition timing scheme for a single module. DRDY: Data ready signal of AFE sampling all channels with 1 kSPS; NStep #: iteration of NIRS administration routine for one complete measurement for all active channels (here: 4); EEG: EA+DS: Exponential averaging and Downsampling of EEG signal; S&S: Sample and switch ON/OFF new wavelengths ($\lambda$)/ LEDs (L); Assign & L-I: Assignment of emitter–detector combinations to channels and phase-sensitive demodulation

resistors are placed between electrodes and ADS1299 circuitry, which itself was designed by the manufacturer to conform with the safety regulations for medical electrical equipment.

***3) Hybrid Acquisition, Timing, and Communication:*** To administrate and synchronize the acquisition of both signal types, the AFE and microcontroller ($\mu$C) build a closed loop in the M3BA architecture. Once a continuous measurement is started, the AFE acquires signals with a sample rate previously set (using an internal oscillator) and indicates complete conversions to the $\mu$C via a data ready (DRDY) signal. The DRDY signals trigger data retrieval and TDMA control of the NIR emitters by the $\mu$C. Fig. 3 exemplifies such a typical hybrid acquisition cycle of a single M3BA module.

The AFE runs at a fixed sample rate of 1 kSPS (with an input bandwidth of BW $= 262$ Hz); one complete NIRS measurement cycle takes 60 sample (DRDY) events. While the EEG data are continuously saved, exponentially averaged, and downsampled to a user-configurable sample rate of 500 or 250 SPS, the NIRS routine is called every second DRDY iteration. In one NIRS measurement cycle, it subsequently switches twice ($I/II$) through all available emitter states (here five: two LEDs $L_{y=1}$ and $L_{y=2}$ each with two wavelengths $\lambda_{x=1} = 750$ nm and $\lambda_{x=2} = 850$ nm and a dark measurement period). Signals of all photodiodes during one state are simultaneously measured. For one module, each state is sampled six times, where at least the first two samples are discarded during settling of the Si-PD signal ($t_{\text{dwell}} \geq 2$ ms). The last of the acquired samples is saved, assigned, and the next emitter state is activated. Once each 60 ms, when a NIRS measurement cycle is finished, all resulting four measurements of each emitter–detector pair (two active emitter and two dark measurements) are combined in a phase-sensitive demodulation step ($\lambda_x {L_y}^I + \lambda_x {L_y}^{II} - \text{Dark}^I - \text{Dark}^{II}$) for dark current and background radiation subtraction. This results in a NIRS sample rate of $f_{\text{sNIRS}} = 1/60$ ms $= 16.66$ Hz with the NIRS samples being time-locked to the EEG signal.

Since each emitter state is activated two times per measurement cycle, this yields an LED current switching frequency of $f_{\text{switch}} = 33.33$ Hz and its multiples, potentially creating crosstalk into EEG inputs. The aforementioned PCB design minimizes this, and we evaluated the quality of the approach. See Sections II-B2 and III-B2 for the methods and results.

For synchronization of several M3BA modules, one declared master module shares a physical eight-wire parallel interface with the slave modules. Over this interface, all AFEs are synchronized with a shared sample clock provided by one master AFE; NIRS TDMA channel control is administrated and common references are shared.

Each module communicates with a host Notebook or PC via an integrated BTM from ST-Microelectronics (SPBT2632C2A) using serial port profile (SPP). Other processing units that support Bluetooth SPP (like smartphones or tablets) can as well be used for data acquisition. Data between $\mu$C and BTM are transferred via a flow-controlled and ring-buffered USART interface to minimize packet loss.

## B. Hardware Performance Characterization

In this subsection, methods and phantoms used for evaluation of the hybrid architecture are presented. Since the ADS1299 is designed for EEG acquisition and performance details are provided by the manufacturer [27], we focus on the optical (NIRS) and hybrid performances as well as crosstalk characteristics.

***1) Evaluation of NIRS Signal Quality and Phantom:*** The evaluation of the NIRS characteristics was performed employing a solid homogeneous optical phantom with tissue-like scattering and absorption properties, to mimic 1) the total attenuation that occurs in the tissue at a source–detector separation of 30 mm; and 2) the diffuse nature (in terms of its spatial and angular distribution) of light exiting the tissue. We made use of a phantom of known diffuse transmittance that was devised and characterized to assess the responsivity of the detection system of time-domain optical brain imagers [28], [29]. The phantom was a cylindrical slab of thickness 20 mm and diameter 105 mm, made of epoxy resin with $TiO_2$ particles added as a scattering medium and black toner as an absorbing medium, following the recipe published by Swartling *et al.* [30]. Its optical properties at 750 nm were: reduced scattering coefficient 0.53 $\text{mm}^{-1}$, absorption coefficient 0.0126 $\text{mm}^{-1}$, and refractive index 1.55. As a measure of diffuse attenuation, we adopted the optical loss (OL) as defined in the international (IEC/ISO) standard for functional NIRS equipment [31], i.e., as the ratio of the total optical power exiting a circular aperture of specified diameter (8 mm) on the exit side of the phantom and the power injected on the entrance side. In the following, the OL is either given as a ratio or in dB units, where $X$ dB is equivalent to $10^{-X/10}$. The OL of the phantom used was 24.7 dB at 750 nm and 23.5 dB at 850 nm. The tests in the IEC/ISO standard refer to OLs of >40 dB or >60 dB, depending on the particular test, to mimic a typical attenuation for fNIRS. We achieved such values by using additional gray filters.

The tests were performed in a custom experimental setup with one NIR emitter–detector pair and the phantom in transmission geometry, as shown in Fig. 4(a).

The phantom was placed in a black plastic holder, with its bottom surface in direct contact with the fNIRS photodetector. On the top side, the phantom holder case was closed with a custom black two-piece lid (3-D printed) that acted as a rail for an absorbing neutral step filter (15 steps covering an op-

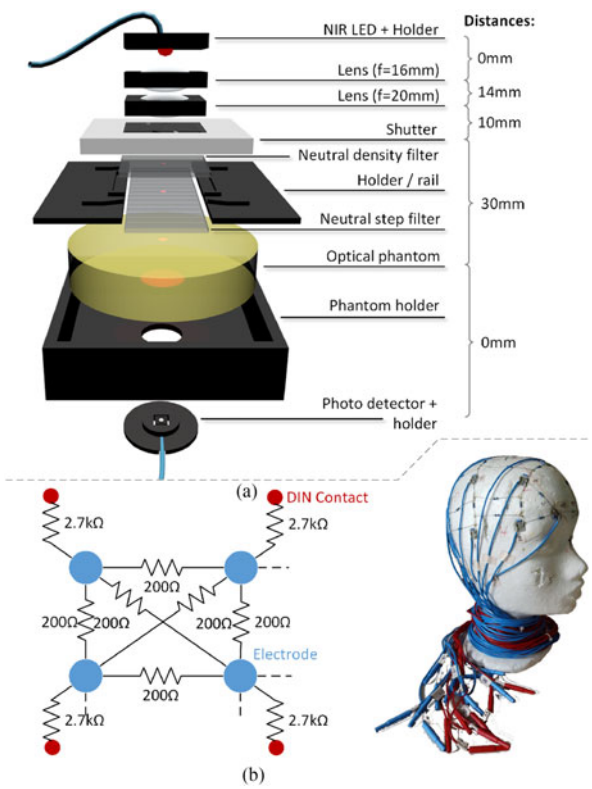


Fig. 4. (a) Experimental setup for NIRS characterization using an optical phantom with neutral step filters. (b) Electrical phantom for crosstalk evaluation of NIRS switching into EEG inputs of M3BA and commercial device.

tical density range of approximately two orders [20 dB]) and additional neutral density glass filters. These filters were used to vary the overall OL. Light from the NIR emitter mounted on top of the structure was imaged onto the phantom (diameter of illuminated spot: 5 mm) by two convex lenses and passed through a controllable optical shutter (type Melles Griot 04 IES 211, controller 04 IPS 850, actuation speed: 17 ms). The shutter was controlled via a M3BA hardware trigger output; shutter (de)activation was acquired and labeled to the acquired NIRS data stream. The attenuation of all used neutral density filters and filter steps was determined independently via power transmission measurements using a supercontinuum laser (SC500-6, Fianium Ltd., U.K.) with acoustooptic tunable filter tuned to 750 and 850 nm, respectively, and a Coherent Fieldmaster power meter with sensor head LM-2.

The following measurements were conducted with an input gain setting of $G = 4$ and an emission level setting of $I = 8$ (8.94 mW @750 nm, 8.34 mW @850 nm):

1) *Drifts/Stability*: At a fixed total OL ($\mathrm{OL}_{750\,\mathrm{nm}} = 47.3$ dB, $\mathrm{OL}_{850\,\mathrm{nm}} = 50.2$ dB), the optical signal was acquired continuously for 15 min twice. For estimation of the continuous drift, the slope and $R^2$ of a linear least-squares fit were calculated.
2) *Signal-to-noise ratio (SNR)/Coefficient of variation (CV) and linearity (LIN) of the instrument:* In a continuous acquisition, after 5-min free-running for warm up, 42 measurements of the NIRS signal in a range of $\mathrm{OL} = 4 \times 10^{-2}$ to $9 \times 10^{-6}$ (26.0 to 69.5 dB) were conducted in approximately 1.5 dB steps. The last 10 s of data (170 samples) were used for the evaluation of each step. During manual filter step transitions, the shutter was closed. For each measurement, the shutter was opened, thus also providing a step response (SR) in the acquired signal $s$. Standard deviation ($\sigma_s$) and mean ($\bar{m}_s$) were calculated for all steps and both acquired wavelengths. CV and SNR were calculated as $\mathrm{CV}_s = \sigma_s/\bar{m}_s$ and $\mathrm{SNR}_s = 20\log(\bar{m}_s/\sigma_s)$. It should be noted that for hardware performance characterization, this SNR is related to the total optical signal, not to the hemoglobin concentration changes derived in fNIRS. For LIN evaluation, slopes and $R^2$ values of linear least squares regression fits on the $\bar{m}_s$ for each wavelength were calculated.
3) *NIR emitter power*: The continuously emitted radiant power (no switching) for each wavelength was measured with a Coherent Fieldmaster power meter with sensor head LM-2. The LED was mounted in such a way that the illuminated area was fully covered by the sensor's photosensitive area. The emitted power at six different current levels ((5–10) $\times$ 10 mA) and the illuminated area on the optode surface were measured to determine the incident intensity at the subject's scalp.
4) *NIR emitter spectrum*: The spectra of the NIR emitters for both wavelengths and different current levels were measured with an Avantes AvaSpec 3648 spectrometer with an integration time of $t_I = 50$ ms and averaging over 200 measurements. The NIR light was attenuated by 32.4 dB (750 nm) and 33.3 dB (850 nm) using neutral density filters. The measured spectra were corrected by the previously determined calibrated spectral sensitivity and by dark measurements. Spectral dependence on emission directions due to varying local semiconductor characteristics was evaluated by measuring the spectra at different tilts of the emitter. Peak wavelengths (PWs) were calculated by a maximum search of a Gaussian fitted to the top 10% area of each spectrum. Maximum PW shifts over all intensities were determined ($\Delta\mathrm{PW}_{\lambda,\max}$). The full-width at half-maximum (FWHM) of the spectral power distribution was calculated as the difference of the wavelength between the two points whose corresponding power values are equal and 3 dB lower than the values at each PW.
5) *Noise equivalent power (NEP)*: For determination of the NEP of the NIRS part of the instrument, 60 s (1000 samples) of the signal were acquired for each input gain $G$, while the fNIRS emitters were active, but the detectors were put into an opaque box with no incident light. Using the OPT101 responsivities $R_{\lambda=750} = 0.55\,\mathrm{V}/\mu\mathrm{W}$ and $R_{\lambda=850} = 0.60\,\mathrm{V}/\mu\mathrm{W}$, the signal mean $\bar{m}_{G,\lambda}$, and standard deviation $\sigma_{G,\lambda}$, the NEP was then calculated for the full input bandwidth (262 Hz) as $\mathrm{NEP}_{G,\lambda} = \frac{\bar{m}_{G,\lambda}+\sigma_{G,\lambda}}{R_\lambda \cdot G}$.

***2) Evaluation of Electrical Signal Quality and Phantom:*** For comparative measurements of NIRS switching crosstalk into EEG inputs, we used a resistor network made from metal film 0.1 % resistors as shown in Fig. 4(b). The phantom consists of a polystyrene head covered with a resistive net-

work with nodes ("electrodes") at 10–20 EEG positions, which can be accessed via DIN-electrode jacks. The resistive network simulates electrode-to-skin impedance (2.7 kΩ) and between-electrode skin conduction (200 Ω). Clearly, this network does not have the same AC properties as the human scalp probed with EEG. However, it allows well-defined comparative measurements which rather favor nonhybrid systems, as electrode impedances are low and equal and the network topology homogeneous: Inhomogeneities in realistic applications, e.g., varying electrode impedances (resulting in a worse common-mode rejection), are likely to have a lesser effect in optimized hybrid systems with common ground than in combined stand-alone instrumentation approaches. At position F8, voltage-divided sine signals with $A = 150\ \mu$V and $f_s = \{1{,}10{,}100\}$ Hz from an Agilent 3500B signal generator were fed into the network. The two NIR emitters of one M3BA module were placed between Fz&Cz and F3&C3 and either active or inactive ($a = 0, 1$). Signals were measured at positions $p = \{Cz, Fz, C3, F3, F8\}$ against a common reference (GND) at T5. Each 70-s measurement $m_{f,p,a}$ was repeated with both the M3BA module (@500 SPS) and with a commercial reference EEG amplifier for comparison (COM, g-tec USB Amp, 2009, @512 SPS). For evaluation of the crosstalk, the FFT power spectra of the last 60 s of $m_{f,p,a}$ were calculated and normalized for the peak power at $f_s$ to be one: $P_{\text{norm}}(f_s) = 1$. Then, for $i = 1...7$, the normalized noise powers of multiples of the NIRS switching frequency $f_{\text{switch}}$ were extracted and summed up $P_{\text{noise}} = \sum P_{\text{norm}}(i \cdot f_{\text{switch}} \pm 0.155)$. This allows a comparison of the strength of NIRS switching noise introduced into the EEG signal.

Crosstalk/electrical noise from NIRS currents can be introduced to the inputs on the PCB itself when the instrument layout, for instance, current return design, is not optimal—but can also be coupled in by fields between the EEG-electrode and NIRS optode wires. To differentiate between both types, we used a feature of the ADS1299 AFE that allows the input multiplexer to internally shorten the inputs to measure the input-referred noise. For active and nonactive NIRS ($I = 8$) and all PGA gains $G = 1 - 24$, the input referred noise was determined by calculation of the standard deviation of 2000 samples (@500 SPS) for each condition.

To verify the desired EEG input linearity and cutoff (mainly influenced by the AFE input bandwidth and implemented exponential averaging on the $\mu$C), the input frequency response was evaluated by acquiring a linear 5-s sweep from 0.1 Hz to 2 kHz with constant step width and 100 $\text{mV}_{\text{pp}}$ and 100 $\mu\text{V}_{\text{pp}}$ amplitudes, generated by the Agilent 3500B. The frequency response was extracted by applying a polynomial curve fit with order 21 through the Hilbert envelope of the acquired raw sweep signal.

All experiments were conducted in a magnetically and electrically shielded room (two-mu metalayer Ak3b, Vakuumschmelze, Hanau).

### C. Physiological Data—Human Subject Studies

For a better characterization of the architecture and instrument performance, this paper is focused on hardware characteristics. However, a proof of functionality by successful acquisition of the targeted biosignals is desirable. While further improving sensitivity, the M3BA fNIRS emitter–detector design is based on the core units of the openNIRS design (NIR wavelength selection, NIR light emission, and detection circuitry and components) that has been validated with successful brain activity measurements in a mental-arithmetic-based $N = 12$ BCI study, documented in [17]. For the EEG functionality and multimodal acquisition, the following human subject studies were conducted according to the declaration of Helsinki and approved by institutional ethics committees. We performed the experiments on a few subjects only, sufficient for a first proof of functionality. All participants were comprehensively informed and gave written consent before the experiment.

***1) EEG: Comparative Measurements of Auditory Evoked Potentials (AEPs):*** To characterize the practical capabilities of EEG amplifiers, it is often the best to perform evoked potential measurements with human subjects. Pure technical parameters can be easily determined using proper test equipment, but for EEG signal generation phantoms are rarely known. Instead, human subject data are considered the gold standard. We followed this qualitative approach and measured AEPs [32] on five right-handed subjects (three males, two females, avg. age $26 \pm 2y$.) stimulating the left ear with 1 kHz sine tones of 400-ms duration. Tones were delivered using an Etymotic ER-30 insert earphone and an RME HDSP 9632 soundcard. Tones had 92-dB SPL as measured with a Bruel&Kjaer type 4153 artificial ear. In total, 300 tones were delivered with a randomized interstimulus interval of 1.5–2.5 s. This resulted in an experiment time of roughly 12 min and after 6 min, subjects were notified of half time. Each subject was measured with the M3BA and a commercial g.USBamp EEG amplifier (www.gtec.at). The electrode plugs were moved between device inputs and the session lasted 30 min (12 + 12 + change of EEG plugs) in total for both amplifiers. The sequence of M3BA and g.USBamp was randomized between subjects. The signals were acquired over the left fronto-parietal region at the 10–20 positions C3, F3, T3, and T5 and measured against the right mastoid with GND (DRL) placed at Fpz. AgCl ring electrodes were used with gel and impedances were below 10k. The recorded signals were digitally filtered with a zero delay bandpass of 0.1–45 Hz and fourth-order Butterworth characteristics. Epochs were baseline corrected in a 100-ms prestimulus interval and then averaged for each subject and channel to obtain the AEP. The obtained AEPs were compared to literature results [32] with respect to amplitude and latency of the N1-P2 complex.

***2) Multimodal Raw Data Example:*** For qualitative example data and validation of the multimodal mobile acquisition capabilities of the M3BA instrument, we performed several simple ten trial experiments on one subject: One single M3BA module was fixated to a 10–20 EEG cap (easycap) simultaneously measuring EEG (@500 Hz) with wet electrodes at positions O1, O2, Cz, and Fp2, one channel of ECG (Einthoven 2 derivation), accelerometer data, and four fNIRS channels (@16.6 Hz). fNIRS emitters were placed at AF3 and AF7, and detectors at F5 and Fp1, resulting in approximately 30-mm emitter detector distances. The subject was asked to stand, close eyes, and take a deep breath when a first beep sound was played and to open

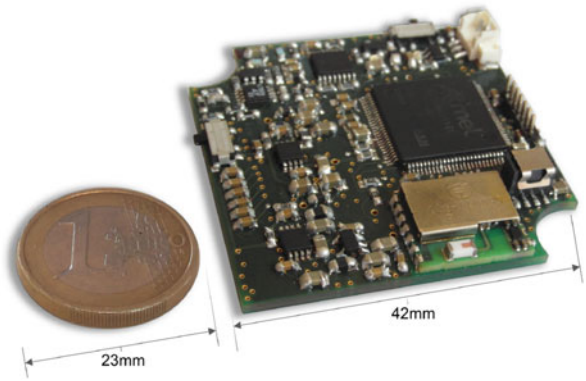


Fig. 5. Stand-alone M3BA module without battery.

eyes after a second beep sound after 10 s. Other experiments also included sitting down, standing up, walking, and turning around. Example data for these longer trials can be found in a more comprehensive figure in the supplementary material. For a better assessment of the raw data quality, only little processing was performed in MATLAB: EEG and ECG channels were digitally filtered with a sixth-order zero delay 0.1–45-Hz Butterworth bandpass. For alpha-band power estimation during eyes closed, the average of the Hilbert envelopes of the bandpass filtered (Butterworth second-order, 10–13 Hz) signals of O1 and O2 were calculated. fNIRS $O_2$Hb and HHb concentration changes were calculated from the raw optical signal using effective extinction coefficients [33] of the measured LED spectra and HOMER2 [34] software and were then baseline corrected by mean subtraction.

## III. Results

### A. Instrument

The M3BA architecture was implemented successfully in a highly miniaturized design for precision EEG, EMG, ECG, and fNIRS acquisition, which can be used—among others—for WBSN-based hybrid BCI scenarios. The dimensions of one fully stand-alone M3BA module (see Fig. 5) are merely $4.2 \times 4.2 \times 0.6\,\text{cm}^3$. This allows a flexible integration in different mechanical setups and head-and-body gears. When optodes are directly connected to the module's edges, NIRS source–detector distance is 35 mm, otherwise freely configurable. Different sizes and capacities of Li-ion batteries can be connected via a standard connector: with a current consumption of <100 mA (all features active), a module runs more than 3 h on a tiny $28 \times 34 \times 2\,\text{mm}^3$ (300 mAh) Li-ion battery, and more than 18 h on a standard mobile phone battery.

Table I summarizes the system characteristics of the stand-alone M3BA modules. In the subsequent sections, results from the technical tests and physiological recordings will be described in more detail.

TABLE I
System Characteristic Overview

| | | | |
|---|---|---|---|
| EEG/EMG/ECG/... | | | |
| # of Channels: | $4+2$ | Resolution: | 24 Bit |
| Sample Rates: | 500\|250 Hz | Common Mode RR: | −110 dB |
| Inp. ref. Noise: | 1.39\|0.98 $\mu\text{V}_{\text{pp}}$ | Input PGA: | $G = 1-24$ |
| Inp. Bandwidth: | 210\|100 Hz | Config. Driven Right Leg (DRL) | |
| fNIRS | | | |
| # of Channels: | $4+2$ | Resolution: | 24 Bit |
| Sample Rate: | 16.6 Hz | Wavelengths: | 750\|850 nm |
| Emitter lvl.: | $I = 5-10$ | NEP: | 5.92\|4.77 $\text{pW}_{\text{pp}}$ |
| Input PGA: | $G = 1-24$ | SiPD Respons.: | 0.55\|0.6 $\frac{\text{V}}{\mu\text{W}}$ |
| Optical Drift: | $<1.6\ \frac{\text{ppm}}{s}$ | $\Delta\text{PW}_{\text{max}}$: | 4.75\|3.75 nm |
| Optode Dist.: | 35 mm/conf. | FWHM: | 16.6\|21.4 nm |
| SNR ($10^4$ OL): | 66 dB | Intensities$_{750\,\text{nm}}$: | 0.07–0.14 $\frac{\text{mW}}{\text{mm}^2}$ |
| SNR ($10^6$ OL): | 40 dB | Intensities$_{850\,\text{nm}}$: | 0.07–0.13 $\frac{\text{mW}}{\text{mm}^2}$ |
| Full linearity ($10^{-2} - 10^{-7}$ OL) | | Digital Lock-In Amplification | |
| Accelerometer | | | |
| # of Channels: | $x, y, z$ | Resolution: | 10–13 Bit |
| # Sample Rate: | $0.1-1$ kHz | Ranges: | ±2,4,8,16 g |
| General | | | |
| Power consumption: <360 mW | | Li-Ion Cell (replacable) + charger | |
| Bluetooth range: Indoor 5 m | | Modularity: Up to 4 modules | |
| Hardware trigger precision: $2 \pm 1$ smpl | | | |

### B. Performance Characterization

**1) Optical Characteristics:** The drift measurements revealed the need for a warm-up time of maximum 5 min after switching ON, in which the emitted 850-nm power settles by 1.7%. After that, the optical signals drifted less than 27.5 nV/s, which in relation to the signal amplitude at 40 dB OL is less than 1.6 ppm/s.

1) *Linearity:* The device showed very distinct linearity [see Fig. 6(a)] for both wavelengths (slopes $S_{750} = 0.996, S_{850} = 1.005$, correlation coefficient $R^2_{750|850} = 0.999$) over the full tested optical range.
2) *CV and SNR:* The evaluation of CV and SNR for both wavelengths [see Fig. 6(b)] yielded predominantly constant values (CV $< 0.001$, SNR $> 60$ dB) for low attenuation OL $< 5 \times 10^{-4}$ and linearly increasing CV/decreasing SNR above OL $= 5 \times 10^{-4}$. Even at very high OLs in the range of $10^{-7}$, the SNR is about 20 dB, indicating that small changes in optical power occurring in fNIRS experiments can still be measured.
3) *Step responses* measured with the shutter for all OL configurations showed a settling of the signal within one fNIRS sample (60 ms) without further oscillations.
4) *NIR emitter power and spectrum:* The normalized spectra of the NIR emitters are shown in Fig. 6(c). Tilting experiments did not show a significant dependence between spectrum and tilt of the LED relative to the measurement probe. The spectra measured for all six implemented intensity levels show a slight shift toward higher PWs with higher illumination intensities ($\Delta\text{PW}_{750,\text{max}} = 4.75$ nm, $\Delta\text{PW}_{850,\text{max}} = 3.75$ nm). Changes in the FWHM for both wavelengths are marginal ($\Delta\text{FWHM}_{\text{max}} = 0.75$ nm). Due to the TDMA, the effectively emitted intensities during fNIRS acquisition are 1/5 of the ones measured during continuous emission.

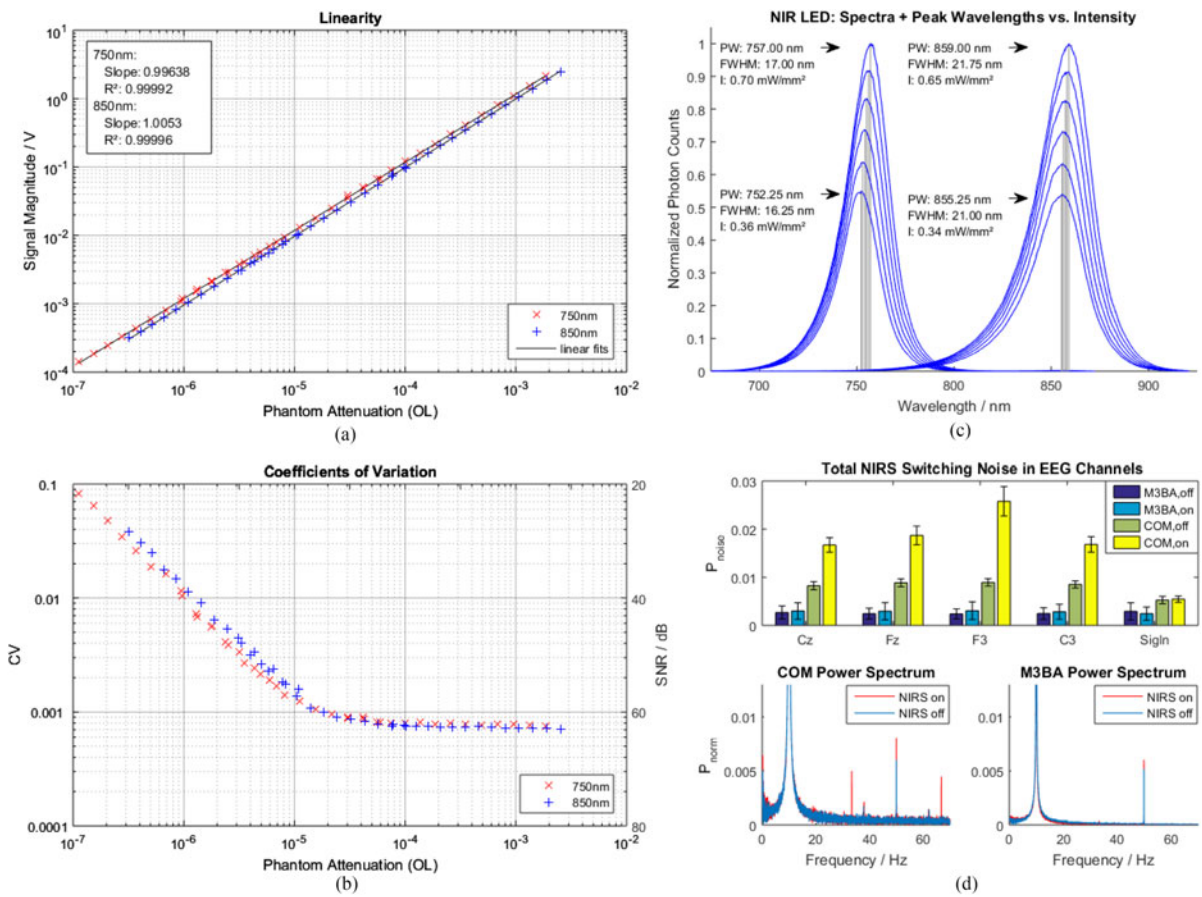


Fig. 6. Performance characteristics for fNIRS/EEG unit. (a) Linearity of measured optical NIRS signals over the whole range of OL. (b) Coefficient of variation/SNR of NIRS measurements. (c) NIR emitter spectra for six intensity levels (I), PW, FWHM emitted intensities for minimum and maximum level. (d) NIRS switching noise in EEG-measurements. (Bottom) Normalized FFT-Power spectra exemplify presence of $f_{\text{switch}} = 33.3$ Hz and its multiples in the signals measured with the comparative (COM) device and absence in M3BA. (Top) Sums of normalized switching noise fractions for active (ON) and inactive (OFF) fNIRS in the signals of several electrodes.

5) *NEP:* The NEP of the detector circuit (the threshold at which incident light of a target wavelength completely drowns in noise) for all PGA gain levels was measured to be in the order of $\text{NEP}_{\text{min},850} = 4.77$ pW to $\text{NEP}_{\text{max},750} = 5.92$ pW incident power.

***2) Electrical Characteristics:*** Evaluation results for the electrical NIRS switching crosstalk into EEG: Comparative measurements of input referred noise and power supply voltages during active and inactive NIRS revealed an increase of the high-precision bipolar supply voltage noise from $6.6\,\mu\text{V}_{\text{rms}}$ to $21.4\,\mu\text{V}_{\text{rms}}$ (262 Hz − BW) with the NIRS active. However, the input-referred noise of the EEG channels for all PGA settings stayed in line with the manufacturers data ($<0.28\,\mu\text{V}_{\text{rms}}$ at 1 kSPS with 262-Hz bandwidth and $G = 24$) for both active and inactive NIRS conditions. The crosstalk evaluation on the electrical phantom with both the M3BA and comparative device (COM) [see Fig. 6(d)] showed distinct peaks at $f_{\text{switch}}$ and its higher harmonics in the FFT-power spectra for all test signals measured with the comparative device. Measured with the M3BA module, they are almost completely indiscernible from the generally lower noise floor. This is also reflected in the normalized sums of the fractions of power of $f_{\text{switch}}$ and its multiples in measurements during active and inactive NIRS: In the M3BA module, these show no significant deviations and are smaller than 0.003. In the nonhybrid setup with the comparative device, a significant increase between conditions and a noise level up to one order of magnitude (0.028) higher than in the M3BA, as well as a spatial dependence were observed. The higher noise of the COM may be due to longer cable length and unavoidable ground loops as the combined setup was not optimized for low noise performance.

The input frequency responses of the M3BA EEG unit for both configurations (250/500 SPS) confirmed flatness (<0.1 dB) in the passband and the cutoffs set by exponential averaging ($f_{cEA500} = 210$ Hz, $f_{cEA250} = 100$ Hz) and AFE bandwidth ($f_{c\text{BW}} = 262$ Hz).

## C. Physiological Data—Qualitative Results

***1) EEG: AEPs:*** The signals of one out of five subjects were discarded due to very high mains hum in the comparative measurement using the COM instead of the M3BA EEG channels. Signal analysis showed distinct N1-P2 peaks typical for AEPs in the EEG signals of all the remaining four subjects.

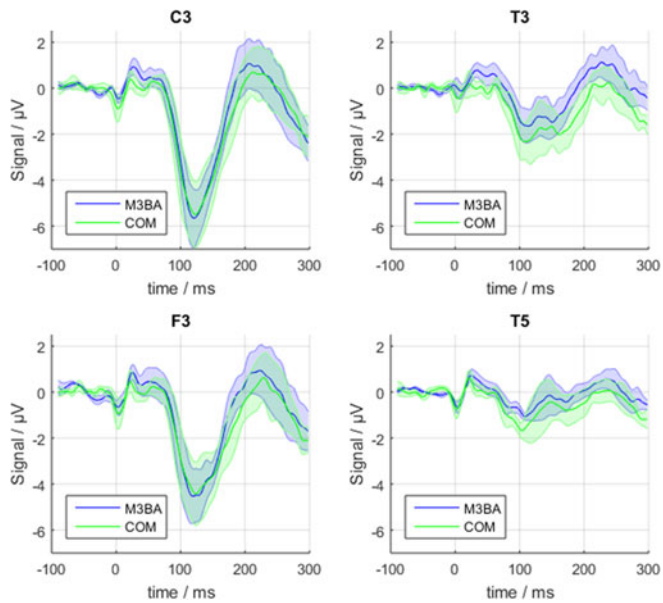


Fig. 7. N100 comparative results between M3BA and commercial (COM) device. Solid lines are signals averaged over all subjects, shaded error bars indicate standard error of the mean (SEM) between subjects for each channel

Here, the positions C3 and F3 showed strong N100 amplitudes, where less typical positions (T3 and T5) showed less distinct signals, as expected. Fig. 7 shows the signals of both devices for each channel averaged over all subjects for comparison. The characteristics of the N1-P2 complex in the signals (timing, amplitude, and shape) indicate that the M3BA performs like a standard precision EEG recording unit.

***2) Raw Multimodal Example:*** Fig. 8 shows a typical single trial of the raw multimodal dataset acquired in the qualitative experiment with a standing subject using one M3BA module. For similar data from an experiment with a freely moving subject, refer to the supplementary material.

O1, O2, and Cz show clear alpha activity during eyes closed (10–20 s); Fp2 shows typical eye blinking artifacts. Deep breathing in and out is clearly visible in the accelerometer signal. Also, the deep breath impacts the ECG heart rate and R-wave amplitude as well as the overall fNIRS signals. The fNIRS signals show the typically stronger pulse waves in $O_2$Hb compared to HHb, which are also clearly correlated to the electrical activity of the heart in the ECG.

## IV. Discussion and Outlook

We here performed a systematic evaluation of our novel multimodal miniaturized device by performance measurements using an optical and an electrical phantom and internal features of the AFE. EEG functionality was demonstrated in an $N = 4$ AEP *in-vivo* study with both the new and a commercial reference instrument and showed the expected characteristic N1-P2 signal amplitudes and shapes. Validation of the basic openNIRS functionality was carried out in [17] by a mental arithmetics brain activation user study. Multimodal acquisition was validated by a qualitative raw data experiment simultaneously acquiring fNIRS, EEG, ECG and acceleration data. The system performance tests demonstrated excellent linearity, low optical drift, and very low noise levels among others. The noise characterization revealed that between 20–50 dB OL, the CV remains constant with values lower than $0.1\%$. This noise component can be attributed to the LED light source; signal as well as noise are proportionally attenuated by the phantom, as long as photon noise can be neglected. Above 50-dB OL, CV linearly increases with an approximate slope of 1, which is indicative of the domination of a signal-independent noise component. Extrapolating the course to 80-dB OL yields CV $\approx 1$ for a signal magnitude in the order of $10\,\mu$V, which coincides with the manufacturer's data for the photodiode's dark noise in the used bandwidth ($15\,\mu$V–262 Hz BW). This is also in accord with the measured NEP values in the order of $10^{-12}$ W, when considering the incident optical LED power of $10^{-3}$ W, an OL of $10^{-8}$, additional losses in the optical path, and the fact that the actual detector area (5 mm$^2$) is smaller than the area of the 8-mm-diameter aperture used in the definition of the OL. We, therefore, assume that the signal-independent noise component is the photodetector's thermal noise on which future attempts to improve performance can focus.

On the fNIRS side, the M3BA architecture improves the openNIRS design by

1) switching from analog-to-digital lock-in amplification and by that removing the attenuation $A$ due to phase shifts (formerly: $A = 0.874$), which increases the SNR by approximately 1.16 dB and decreases the number of analog components as potential noise sources in the detection path;
2) stand-alone integration of all hardware into one single unit;
3) detector parallelization;
4) by better electrical decoupling and overall noise minimization (supplies, decoupling, amplification, and conversion).

The NEP for optical measurements was improved by three orders of magnitude (M3BA: $pW_{pp}$, openNIRS: $nW_{pp}$).

To achieve the desired high-performance characteristics in all modalities, we took great care to minimize noise and crosstalk, by optimizing the mixed-circuit multilayer and multipower supply layout for the AFE—$\mu$C unit. Crosstalk experiments demonstrated a significantly lower impact of fNIRS switching in the EEG inputs of the instrument than the comparative EEG device. Using LEDs and SiPDs for the NIR light emission and detection, we were able to minimize size, power consumption and supply voltages, thereby also increasing safety compared to laser and avalanche photodiode designs. The M3BA unit is supplied with a single 3.7-V Li-ion cell that can be recharged onboard via USB and that can be exchanged by a different-capacity $C_{\text{batt}}$ cell according to runtime required ($t_{\text{run}} \approx \frac{C_{\text{batt}}}{100\,\text{mAh}} h$).

The TDMA use of the fNIRS channels presents a drawback in terms of sampling rate for simultaneous use of several interconnected modules. As depicted in the timing scheme in Fig. 3, due to several unused fNIRS samples in the single module case, for up to two modules, a sampling rate of 16.6 Hz is supported. For each addition module, the sampling rate needs to be decreased

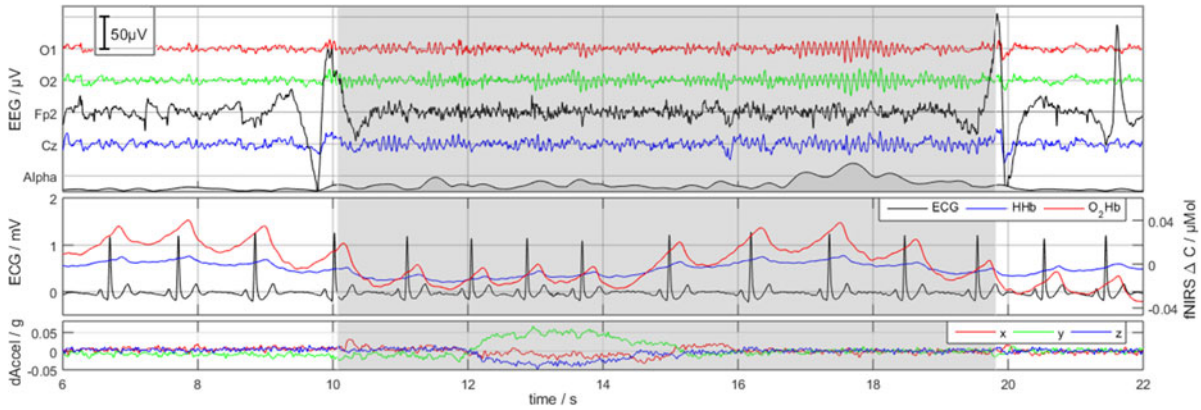


Fig. 8. Synchronously recorded raw multimodal data from a standing subject during deep breath ($t = 12$ s) and eyes open/closed ($t = 10$ s/20 s): EEG channels and alpha power (top), ECG and fNIRS signals (only Ch1 (AF3-F5) for better overview) (mid) and accelerometer signal (bottom). Some typical dependencies between modalities are already observable in the raw ECG, fNIRS and accelerometer signals (R- and pulse wave correlation, ECG/fNIRS modulation by breathing (accelerometer).

due to the TDMA. If necessary in the future, this could be solved by simultaneous illumination with sine-modulated light at different frequencies, although this significantly increases power consumption. Another pitfall arises, when two or more persons, all wearing several M3BA modules in a WBAN scenario, meet at close distances. The interference introduced by the number of Bluetooth transmitters is likely to lead to a high number of lost packages that cannot be buffered. For such scenarios, there are currently no optimal solutions regarding wireless infrastructure. If the modules were to be used in such a setting, other transmission standards like ZigBee (IEEE 802.15.4) and WBAN (IEEE 802.15.6) or even completely new standards could be taken into consideration.

The presented M3BA architecture and instruments enable a wide range of new approaches in the fields of multimodal mobile and wearable BCI, and neurotechnology. For robust unobtrusive use of the instrument, headgear and sensors will have to be tailored to application- and scenario-specific requirements in order to provide mechanical stability and high signal quality. Examples for such unobtrusive wearable sensor solutions are in-ear or around-the-ear EEG [35], [36]. The M3BA architecture provides the necessary flexibility for integration and customization. Furthermore, the high ADS1299 input impedance ($1\,\mathrm{T}\Omega$) and common-mode rejection ratio ($-110$ dB) allow the use of both wet or dry electrodes. Bioelectrical (e.g., EEG) and fNIRS channels are typically spatially separated. For locally combined use (using wet electrodes), clear high-viscosity electrolyte gel allows both electrical contact and preparation (brushing aside and fixating hair) without significantly affecting optical signals. Aside from typical procedures for applying fNIRS on haired regions (e.g., brushing aside hair under the optodes), our next steps with the M3BA modules will include various approaches for robust and spring-loaded mechanical headgear and optodes for all regions of the head utilizing our approach from [17]. Software implementation of the ADS1299 current source/sink peripherals will enable AC lead-off detection and online electrode impedance measurement. Integrating these next steps, we will use the M3BA instrumentation in new hybrid mobile multimodal BCI studies in the near future.

## V. Conclusion

We successfully implemented a so far nonexistent hybrid biosignal acquisition architecture for BCI and neurotechnology applications that incorporates modularity, mobility, miniaturization, multimodality, and scalability, with desired additional features such as phase-sensitive detection and reconfigurable references. The architecture, in part inspired by a next-generation vision of our previously published openNIRS technology, integrates fNIRS with high-precision biopotential measurements utilizing a shared AFE, thereby saving space, costs, and providing high signal quality and precision. Since the design is also based on a powerful microcontroller, the user can easily and quickly change, implement, and increase the complexity of programs running on the module. Thus, new approaches such as decentralized online feature extraction, adaption, and filtering on the modules themselves become possible. These then enable use in wireless tactile scenarios, where context and bandwidth availability on the wireless infrastructure are taken into account in providing and processing of sensor information.

The design principles put forward in this paper are also applicable to other research areas than that of hybrid mobile BCIs. By providing both architecture details and performance characteristics of our design for miniaturized high-precision hybrid biosignal acquisition, we hope to facilitate new hybrid approaches by other research groups in various fields.

## Acknowledgment

The authors would like to thank Dr. M. Grube for her proofreading support.

## References

[1] J. Andreu-Perez *et al.*, "From wearable sensors to smart implants—Toward pervasive and personalized healthcare," *IEEE Trans. Biomed. Eng.*, vol. 62, no. 12, pp. 2750–2762, Dec. 2015.

[2] Y.-L. Zheng *et al.*, "Unobtrusive sensing and wearable devices for health informatics," *IEEE Trans. Biomed. Eng.*, vol. 61, no. 5, pp. 1538–1554, May 2014.

[3] Müller-Putz *et al.*, "Towards noninvasive hybrid brain computer interfaces: Framework, practice, clinical application, and beyond," *Proc. IEEE*, vol. 103, no. 6, pp. 926–943, Jun. 2015.

[4] S. Fazli *et al.*, "Learning from more than one data source: Data fusion techniques for sensorimotor rhythm-based brain-computer interfaces," *Proc. IEEE*, vol. 103, no. 6, pp. 891–906, 2015.
[5] S. Fazli *et al.*, "Enhanced performance by a hybrid NIRS-EEG brain computer interface," *Neuroimage*, vol. 59, no. 1, pp. 519–529, 2012.
[6] G. Pfurtscheller *et al.*, "The hybrid BCI," *Frontiers Neurosci.*, vol. 4, p. 30, 2010.
[7] B. Z. Allison *et al.*, "Toward smarter BCIs: Extending BCIs through hybridization and intelligent control," *J. Neural Eng.*, vol. 9, no. 1, 2012, Art. no. 013001.
[8] R. Parasuraman, "Neuroergonomics: Research and practice," *Theoretical Issues Ergonomics Sci.*, vol. 4, no. 1–2, pp. 5–20, 2003.
[9] R. Parasuraman, "Neuroergonomics brain, cognition, and performance at work," *Current Directions Psychol. Sci.*, vol. 20, no. 3, pp. 181–186, 2011.
[10] K.-R. Müller *et al.*, "Machine learning for real-time single-trial EEG-analysis: From brain-computer interfacing to mental state monitoring," *J. Neurosci. Methods*, vol. 167, no. 1, pp. 82–90, 2008.
[11] B. Blankertz *et al.*, "The Berlin brain-computer interface: Non-medical uses of BCI technology," *Frontiers Neurosci.*, vol. 4, 2010, Art. no. 198.
[12] T. Zander and C. Kothe, "Towards passive brain–computer interfaces: applying BCI technology to human–machine systems in general," *J. Neural Eng.*, vol. 8, no. 2, 2011, Art. no. 025005.
[13] S. Debener *et al.*, "How about taking a low-cost, small, and wireless eeg for a walk?" *Psychophysiology*, vol. 49, no. 11, pp. 1617–1621, 2012.
[14] H. Ayaz *et al.*, "Continuous monitoring of brain dynamics with functional near infrared spectroscopy as a tool for neuroergonomic research: Empirical examples and a technological development," *Frontiers Human Neurosci.*, vol. 7, 2013, Art. no. 871.
[15] H. Atsumori *et al.*, "Development of a multi-channel, portable optical topography system," in *Proc. 29th Annu. Int. Conf. IEEE Eng. Med. Biol. Soc.*, 2007, pp. 3362–3364.
[16] F. Scholkmann *et al.*, "A review on continuous wave functional near-infrared spectroscopy and imaging instrumentation and methodology," *Neuroimage*, vol. 85, pp. 6–27, 2014.
[17] A. von Lühmann *et al.*, "Towards a wireless open source instrument: functional near-infrared spectroscopy in mobile neuroergonomics and BCI applications," *Front. Human Neurosci.*, vol. 9, 2015, Art. no. 617.
[18] B. Koo *et al.*, "A hybrid NIRS-EEG system for self-paced brain computer interface with online motor imagery," *J. Neurosci. Methods*, vol. 244, pp. 26–32, 2015.
[19] E. Lareau *et al.*, "Near infrared spectrometer combined with multichannel eeg for functional brain imaging," in *Proc. 5th Int. Symp. Med. Inf. Commun. Technol.*, 2011, pp. 122–126.
[20] M. Sawan *et al.*, "Wireless recording systems: From noninvasive EEG-NIRS to invasive EEG devices," *IEEE Trans. Biomed. Circuits Syst.*, vol. 7, no. 2, pp. 186–195, Apr. 2013.
[21] Q. Zhang *et al.*, "Twenty-four-hour ambulatory recording of cerebral hemodynamics, systemic hemodynamics, electrocardiography, and actigraphy during peoples daily activities," *J. Biomed. Opt.*, vol. 19, no. 4, 2014, Art. no. 047003.
[22] J. Safaie *et al.*, "Toward a fully integrated wireless wearable EEG-NIRS bimodal acquisition system," *J. Neural Eng.*, vol. 10, no. 5, 2013, Art. no. 056001.
[23] V. D. Calhoun "A review of group ICA for fMRI data and ICA for joint inference of imaging, genetic, and ERP data," *Neuroimage*, vol. 45, no. 1, pp. S163–S172, 2009.
[24] F. Bießmann *et al.*, " Temporal kernel CCA and its application in multimodal neuronal data analysis," *Mach. Learn.*, vol. 79, no. 1–2, pp. 5–27, 2010.
[25] S. Dähne *et al.*, "Multivariate machine learning methods for fusing functional multimodal neuroimaging data," *Proc. IEEE*, vol. 103, no. 9, pp. 1507–1530, Sep. 2015.
[26] S. Dähne *et al.*, "Integration of multivariate data streams with bandpower signals," *IEEE Trans. Multimedia*, vol. 15, no. 5, pp. 1001–1013, Aug 2013.
[27] *Datasheet: ADS1299 Low-Noise, 8-Channel, 24-Bit Analog Front-End for Biopotential Measurements*, Texas Instrum., Dallas, TX, USA, 2012. [Online]. Available: http://www.ti.com/lit/ds/symlink/ads1299.pdf
[28] H. Wabnitz *et al.*, "Performance assessment of time-domain optical brain imagers, part 1: Basic instrumental performance protocol," *J. Biomed. Opt.*, vol. 19, no. 8, 2014, Art. no. 086010.
[29] H. Wabnitz *et al.*, "Characterization of homogeneous tissue phantoms for performance tests in diffuse optics," *Proc. SPIE*, vol. 9700, 2016, Art. no. 970004.
[30] J. Swartling "Comparison of spatially and temporally resolved diffuse-reflectance measurement systems for determination of biomedical optical properties," *Appl. Opt.*, vol. 42, no. 22, pp. 4612–4620, 2003.
[31] *Medical Electrical Equipment—Part 2–71: Particular Requirements for the Basic Safety and Essential Performance of Functional Near-Infrared Spectroscopy (NIRS) Equipment, Std. IEC 80601-2-71:2015*. [Online]. Available: https://webstore.iec.ch/publication/22638
[32] T. W. Picton *et al.*, "Human auditory evoked potentials. I: Evaluation of components," *Electroencephalography Clin. Neurophysiol.*, vol. 36, pp. 179–190, 1974.
[33] Q. Zhang *et al.*, "Experimental comparison of using continuous-wave and frequency-domain diffuse optical imaging systems to detect heterogeneities," in *Proc. Int. Symp. Biomed. Opt.*, 2001, pp. 219–238.
[34] T. J. Huppert *et al.*, "HomER: A review of time-series analysis methods for near-infrared spectroscopy of the brain," *Appl. Opt.*, vol. 48, no. 10, pp. D280–D298, Apr 2009.
[35] D. Looney *et al.*, "An in-the-ear platform for recording electroencephalogram," in *Proc. Annu. Int. Conf. IEEE Eng. Med. Biol. Soc.*, Aug. 2011, pp. 6882–6885.
[36] S. Debener *et al.*, "Unobtrusive ambulatory EEG using a smartphone and flexible printed electrodes around the ear," *Sci. Rep.*, vol. 5, 2015, Art. no. 16743.

**Alexander von Lühmann** received the B.Sc. and M.Sc. degrees in electrical engineering with a focus on biomedical engineering from Karlsruhe Institute of Technology, Karlsruhe, Germany, in 2011 and 2014, respectively. He is currently working toward the Ph.D. degree at Technische Universitt Berlin (TU Berlin), Berlin, Germany.

He directed a research project on a new mobile multimodal brain–computer interface (BCI) concept in 2014. He is also a scholar of the BIMoS Graduate School, TU Berlin. His research interests include the design of new hardware for multimodal biosignal acquisition and machine learning methods for multimodal electroencephalography- and near-infrared-spectroscopy-based BCIs and human–machine interfaces.

**Heidrun Wabnitz** received the Diploma in physics and the Dr.rer.nat. degree from Friedrich Schiller University Jena, Jena, Germany, in 1979 and in 1982, respectively.

She is a Senior Scientist at the Department of Biomedical Optics, Physikalisch-Technische Bundesanstalt (PTB), Berlin, Germany. She joined PTB in 1991, where she focused on diffuse optical imaging and spectroscopy of tissues, in particular related to optical mammography and brain imaging. She is active in the development of time-domain instrumentation, modeling and data analysis, performance characterization of instruments, and standardization.

**Tilmann Sander** received the Dipl. Phys. degree from ETH Zürich, Zürich, Switzerland, in 1992 and the Ph.D. from Imperial College London, London, U.K., in 1996.

He is a Senior Scientist at the Department of Biosignals, Physikalisch-Technische Bundesanstalt, Berlin, Germany. His work is focused on developments both in signal processing and sensor design for biomagnetic applications. He is further interested in software tools for the clinical application of noninvasive brain imaging methods.

**Klaus-Robert Müller** (M'12) studied physics until 1989 and received the Ph.D. degree in computer science from Karlsruhe Institute of Technology, Karlsruhe, Germany, in 1992.

He has been a Professor of computer science at Technische Universität Berlin, Berlin, Germany, since 2006, and, at the same time, the Director of the Bernstein Focus on Neurotechnology Berlin. He was a Research Fellow at the University of Tokyo in 1994–1995. In 1995, he founded the Intelligent Data Analysis group at GMD-FIRST and directed it until 2008. From 1999 to 2006, he was a Professor at the University of Potsdam. His research interests include intelligent data analysis, machine learning, signal processing, and brain–computer interfaces.

Dr. Müller received the SEL Alcatel Communication Award in 2006 and the Berliner Wissenschaftspreis des regierenden Bürgermeisters in 2014. In 2012, he became a member of the German National Academy of Sciences-Leopoldina.